Published in final edited form as:
Graefes Arch Clin Exp Ophthalmol. 2009 August ; 247(8): 1069–1080. doi:10.1007/s00417-009-1044-3.

Developing SDOCT to assess donor human eyes prior to tissue sectioning for research

Ninita H. Brown,
Department of Biomedical Engineering, Duke University, Durham, NC 27708, USA

Anjum F. Koreishi,
Department of Ophthalmology, Duke University Eye Center, Erwin Rd, Durham, NCBox 3802, 27710, USA

Michelle McCall,
Department of Ophthalmology, Duke University Eye Center, Erwin Rd, Durham, NCBox 3802, 27710, USA

Joseph A. Izatt,
Department of Biomedical Engineering, Duke University, Durham, NC 27708, USA. Department of Ophthalmology, Duke University Eye Center, Erwin Rd, Durham, NCBox 3802, 27710, USA

Catherine Bowes Rickman, and
Department of Ophthalmology, Duke University Eye Center, Erwin Rd, Durham, NCBox 3802, 27710, USA. Department of Cell Biology, Duke University Medical Center, Durham, NC 27710, USA

Cynthia A. Toth
Department of Biomedical Engineering, Duke University, Durham, NC 27708, USA. Department of Ophthalmology, Duke University Eye Center, Erwin Rd, Durham, NCBox 3802, 27710, USA

Cynthia A. Toth: cynthia.toth@duke.edu

Abstract

Background—To compare spectral domain optical coherence tomography (SDOCT) cross-sectional images of human central retina obtained from donor eyes with and without age-related macular degeneration (AMD) to corresponding histopathology from light micrographs. To establish the utility of SDOCT for localizing pathology in the posterior eyecup, for identifying ocular disease in donor eyes, or for directing subsequent sectioning of retinal lesions for research.

Methods—Seven consecutive human donor eyes were selected based on age. The eyes, with the anterior segment removed, were imaged by SDOCT with a focusing aspheric lens. Four eyes were from donors with a clinical history of AMD, and three were from age-matched donors with no history of AMD. Histopathological correlation of morphological changes detected in three eyes by SDOCT was obtained for comparison to step serial-sectioned light microscopy images of the formalin-fixed, paraffin-embedded retina. A simplified imaging setup was tested on an enucleated porcine eye for comparison.

Correspondence to: Cynthia A. Toth, cynthia.toth@duke.edu.

The authors have full control of all primary data, and agree to allow Graefe's Archive for Clinical and Experimental Ophthalmology to review their data upon request.

Financial disclosure McCall: Honoraria from Bioptigen Inc., Izatt: Equipment from Bioptigen, Inc., Consultant for Bioptigen, Inc., Licensed technology to Bioptigen, Inc. Toth: Research funding from: Genentech, Sirion Therapeutics, Bioptigen, Inc., Alcon Laboratories, Inc., NC Biotechnology Center; Consultant for Genentech, Licensed technology to Alcon Laboratories.

Results—AMD pathology was detected and localized in four eyes by SDOCT. The SDOCT images correlated with the histopathology observed by light microscopy in each sectioned eye. Pathologies included a subfoveal neovascular lesion with subretinal fluid, peripapillary neovascularization, epiretinal membrane, foveal cyst, choroidal folds, and drusen. Similar imaging was possible with the simplified setup.

Conclusions—SDOCT imaging identified retinal disease of the posterior eyecup in human donor eyes. Pathology detected with SDOCT was verified by light microscopy in three eyes, supporting the utility of SDOCT as a screening tool for research.

Keywords

Age-related macular degeneration; SDOCT; Human donor eyes; Drusen

Introduction

Optical coherence tomography (OCT) is an imaging modality that has been used for over a decade to image the retina [1, 2]. Time-domain OCT images have been correlated with histological analysis of the retina in animal [3–11] and human cadaver [7, 12–15] eye studies. These studies have shown close correlation of tissue layers, for example at sites of laser lesions [16]. There have been a few small animal studies [17, 18] performed using spectral domain OCT (SDOCT), a form of Fourier domain OCT for volumetric imaging. No studies have shown human postmortem pathology correlation with imaging using SDOCT.

In SDOCT, a spectrometer in the detection arm measures the interference light spectrum and converts this data to depth information by Fourier transformation [19–21]. SDOCT is a fast, high-resolution imaging modality previously used to image the human retina in vivo [21–23], with clinical application in posterior eye diseases including glaucoma [24] and age-related macular degeneration (AMD) [25].

AMD is the leading cause of irreversible vision loss in developed countries [26–32]. The clinical findings range from the early stage of AMD, distinguished by the presence of numerous or large (>125 μm) drusen [33], to late-stage AMD, classified as either atrophic (dry) AMD with geographic atrophy or exudative (wet) AMD with choroidal neovascularization [29]. Despite the need for accurate classification, there is a paucity of screening for donor eyes beyond the patient history and gross examination with photography after dissection [34–36]. SDOCT is widely used clinically, and thus can potentially screen the retina of human donor eyes for research. AMD lesions found with SDOCT must first be correlated with histopathology in the human donor eye.

Materials and methods

Tissue preparation

Whole human donor eyes or posterior eyecups were obtained from the North Carolina Eye Bank (Winston-Salem, NC, USA). For each eye, the donor age, sex, death to procurement time, and ocular history (when available) are summarized in Table 1. Eyes 1 and 2 were obtained from the same patient. Eyes 1–4 were obtained from patients with a history of AMD. Eyes 1–4 had the anterior segment (including the lens) removed by the Eye Bank prior to transfer of the tissue. The anterior segment for Eyes 3–7 was removed in our laboratory. In all eyecups, the vitreous was removed and replaced with fresh 1% paraformaldehyde prior to imaging the eyecups. All eyecups were stored in 1% paraformaldehyde at 4°C for at least 8 months prior to SDOCT imaging.

SDOCT imaging

Eyes were imaged using an experimental SDOCT system (developed in the Biomedical Engineering Department at Duke University) shown in Fig. 1. The system was illuminated with a superluminescent diode (SLD, Superlum, Ltd.) source with a center wavelength of 840 nm and full-width at half maximum bandwidth of 49 nm. The system had axial and lateral resolutions of 4.5 μm and 20 μm respectively. The scan rate was 20,000 A scans/second using OCT 1.4 imaging software (Bioptigen, Inc., Durham, NC, USA). There are 2048 pixels per A-scan. An aspheric lens (AC127–019-B, 52.6 diopters in air, Thorlabs Inc.) was used to focus light onto the retina.

Originally, the aspheric lens was mounted in a customized posterior eyecup chamber filled with ~100 ml of 1% paraformaldehyde. A lens tube in the chamber wall held an aspheric lens horizontally in front of the eye cup (Setup 1 in Fig. 1). A removable stage allowed for 3D adjustment of the posterior eyecup within the chamber for imaging. This setup proved to be time-consuming to mount and position the eye. Repeated placement upright in the chamber also resulted in vitreous traction to the retina. As a result, a hand-held SDOCT system (Bioptigen, Inc.) was used in which the eyecup was positioned with the posterior pole downward to avoid manipulation and secondary vitreous traction (Setup 2 in Fig. 1). With the hand-held probe, a pig eyecup was placed in a small beaker of 1% paraformaldehyde with the aspheric lens submerged into the fluid vertically above the eye cup. This SDOCT system is cart-based, with a hand-held scanning and optical head [37]. Although preliminary imaging was taken while manually holding the scanning head, in the final iteration of the experimental setup the hand-held probe and aspheric lens were mounted on a ring stand above the posterior eye cups, in order to image the retina without moving the tissue or introducing motion artifact from hand movement. The images were post-processed with the updated software InVivoVue 1.2 (Bioptigen, Inc.).

Three types of images were taken: summed 10 mm B-scans, 5×5 mm volumetric scans, and 10×10 mm volumetric scans. For the summed 10 mm B-scans, up to 800 repeated B-scans, each comprising 1000 A-scans, were obtained along a scan line across the optic nerve and macula to evaluate the benefit of summed image. The number of repeated B-scans was limited to 800 due to computer memory limitations. From 2 up to 800 of the B-scans were registered and summed using NIH ImageJ [38] (using the StackReg plugin, Biomedical Imaging Group, Swiss Federal Institute of Technology, Lausanne, Switzerland). The noise variance was also calculated from the standard deviation squared of the intensity 50×50 pixel in the background signal. [39]. The variance of different summed images was used to find the optimal number of images to sum. For comparison, an in vivo series of 10 mm B-scans was obtained of the macula in a normal control subject. This living subject was a control patient in an ongoing institutional review board approved clinical study with the SDOCT system. (Informed consent was obtained from the living patient after explanation of the nature and consequences of the study, following the Declaration of Helsinki.) Performing 800 repeated B scans in vivo would not be possible due to eye movement.

For the 5×5 mm volumetric scans, images were centered on either the macula or the optic nerve head with 500 A-scans per 5 mm B-scan and 500 B-scans per 5 mm. Lastly, the 10 mm×10 mm volumetric scans were either centered on the macula or included both the macula and the optic nerve with 1000 A-scans per 10 mm B-scan and 500 or 800 B-scans per 10 mm. The volumetric scans did not contain repeated B-scans due to computer memory limitations.

The SDOCT images were analyzed to identify pathology in each eye. Each B-scan stack was vertically registered using ImageJ [40], then sites of pathology were marked within each B-scan using Amira (Visage Imaging, Inc. Carlsbad, CA, USA) [23]. The stacks were re-

processed to create a summed-voxel projection (SVP). The SVP was produced from collapsing the stack of SDOCT B-scans along the depth axis [23]. Within the SVP, the shadow from the retinal vessels and different reflective properties of the ocular structures translated into a “funduscopic” view of the retina.

Histopathology

In three eyes, after the SDOCT imaging was completed, a square block of tissue including the macula and optic nerve was dissected from the eyecup, approximately matching the SDOCT scanning area. The tissue was processed “with the sclera intact using automated paraffin embedding (Tissue Tek VIP, Sakura Fineteck USA, Inc., Torrance, CA, USA) to decrease tissue shrinkage and retinal detachment during sectioning. In eyes 2 and 3, step serial-sections, 5 μm thick in 50 μm step intervals, were cut vertically from the optic disc to the macula. In eye 7, serial sections, 5 μm thick, were cut horizontally.

Four to six sections were mounted on each slide. Every other slide was stained with either hematoxyloin and eosin or Masson’s trichrome, and then examined with a Zeiss light microscope (Carl Zeiss, Inc., Thornwood, NY, USA). Images were captured digitally using an Axio Cam HRc camera (Carl Zeiss, Inc.) with Axiovision 4.6 software (Carl Zeiss, Inc.) and processed using ImageJ. All sections were stained except for the infrequent dropped sections. In eye 3, the sections were aligned using the retinal arcade arteries, marked using Amira, as landmarks to create a histological summed stack for better correlation to the SDOCT SVP image (Fig. 2).

Results

The SDOCT imaging of donor eyes using the imaging chamber produced clear and useful SVP images when compared to corresponding postmortem fundus photographs taken with a dissecting microscope (Fig. 3). Arrows in Fig. 3 point out the utility of the SVP image (not segmented or processed for contrast enhancement) for mapping anatomy such as the retinal vessels, macula, and optic disc.

In this study, SDOCT imaging of formalin-fixed retinal tissue differed from that of the living eye (Fig. 4). Comparing Fig. 4a and 4c, the fixed tissue had less contrast between retinal layers and greater reflectivity from the inner retinal layers, which diminished some of the signal from deeper structures. The contours and retinal layer thickness was also different in the fixed tissue. The background variance in both the living eye and the fixed eyecups decreased as the number of summed images increased (Fig. 4 and 5). There was little difference in the variance between 100 summed B-scans (Fig. 4e) and 800 summed B-scans (Fig. 4f). As the number of summed images increased, the variance decreased.

Despite the differences in formalin-fixed tissue and the living eye, pathology was readily imaged using SDOCT of the formalin-fixed eyecups as shown in Table 2, which lists SDOCT morphologic findings in the seven eyes with comparison to the histopathology in three eyes.

In eye 2, early AMD was diagnosed 3 years prior to death. The AMD appeared to have progressed to late exudative AMD, based on the postmortem SDOCT images. These images showed a subretinal hyporeflective area consistent with fluid along with a well-defined reflective subfoveal lesion corresponding to a CNV complex measuring a maximum height of 162 μm and base of 2.1 in the temporal to nasal direction ×1.1 mm in the inferior to superior direction (Fig. 6a). Deep choroidal vasculature was also visible on the SDOCT images of this eye (Fig. 6a). Analysis of macular histology revealed a CNV complex with the same contour detected on the SDOCT scans with a maximum height of 130 μm and

width of 1.4 mm in the inferior to superior direction correlating with the SDOCT (Fig. 6b,c). The length of 2.1 mm in the temporal to nasal direction measured with SDOCT could not be confirmed due to tissue loss during sectioning. Overlying the CNV complex were pigmented cells presumed to be from the retinal pigment epithelium (RPE) (Fig. 6c). Although the retinal separation visible on SDOCT may have occurred postmortem, we believe it likely developed in vivo due to the subretinal debris (arrow in Fig. 6b).

For eye 3, the family reported a history of “macular degeneration.” SDOCT imaging revealed abnormal morphology in both the peripapillary region and macula (Figs. 7, 8). SDOCT imaging detected both subretinal “fluid” with mixed hyper- and hyporeflective material above the RPE and an adjacent apparent RPE detachment, suggesting a CNV complex nasal to the nerve. The corresponding light micrographs confirmed the subretinal and sub-RPE serosanguinous fluid (Fig. 7).

In addition to the peripapillary findings in eye 3, the SDOCT images of the macula showed an intraretinal cyst at the fovea and a prominent epiretinal membrane with inner retinal distortion consistent with a macular pucker, all of which were also identified on light micrographs (Fig. 8). Note the retinal cyst was in the outer retinal layers on both the SDOCT images and light micrographs, with only photoreceptor outer segments between the cyst and the RPE (Fig. 8a,b). Away from the fovea, SDOCT images showed a space between the epiretinal membrane and the retina more highly reflective than the vitreous cavity (double arrows, Fig. 8c) that corresponded to a site of preretinal exudates with inflammatory cells visible on the corresponding light micrograph (double arrows, Fig. 8d). Within the macula, a single druse was detected on SDOCT, but could not be found in the light micrographs of the step serial-sectioned tissue.

In eye 7, there was no documented history of AMD, but there was a history of retinal detachment repair with scleral buckle. On gross examination of the eyecup, the optic nerve and surrounding sclera were pressed into the globe, suggesting postmortem distortion. This distortion may have been caused by the encircling scleral buckle at the equator. The SDOCT images showed numerous irregular RPE elevations (Fig. 9a), initially presumed to be drusen; however, when mapped and summed into an SVP, large arcs of choroidal folds could be distinguished from drusen (Fig. 9d). Some drusen were found on SDOCT isolated from the folds (arrows in Fig. 9d) in similar areas as the light micrographs (Fig. 9e). However, tissue separation and distortion of the choroidal layers prevented truly correlating a specific druse on SDOCT with histopathology.

With the hand-held probe SDOCT system, images of a fixed pig eye were taken of a section of the posterior pole using Setup 2. Figure 10 shows an SVP of the retinal vessels. Figure 10b shows a B-scan of retinal detachment. Compared to previous B-scans, the unsummed B-scan image has better distinction in the retinal layers and less background variance due to improved post-imaging processing.

Discussion

High resolution SDOCT imaging of central retinal morphology can be obtained from formalin-fixed human donor posterior eyecups. Postmortem SDOCT imaging found abnormal preretinal, intraretinal and subretinal morphology in order to predict histopathology visible on light micrographs of the corresponding area. The cross-sectional morphology from SDOCT can be mapped to the SVP for two-dimensional localization of pathology. Unexpected pathology such as an epiretinal membrane, subfoveal or peripapillary CNV, identified on SDOCT screening provided useful direction to circumscribe the area for tissue sectioning. Although a custom-built chamber was originally

used, we have demonstrated that in the future imaging can be performed while tissue remains in storage containers.

Postmortem cellular changes and tissue fixation affected SDOCT imaging of the retina. The most prominent change was the diffuse increase in reflectivity of inner retinal layers on OCT. This diffuse increase in reflectivity of inner retinal layers might be related to the prominent edema reported in the post-mortem inner retina [41] or to change in tissue reflectivity in response to fixation, first reported by McCall et al.[42]. Despite these changes and the postmortem separation of the retina in the fixed eye, SDOCT imaging was still capable of defining small peripapillary and macular lesions important for histopathologic studies. SDOCT imaging of posterior eyecups may be a valuable screening tool for staging retinal disease for postmortem research studies prior to gross dissection, processing and sectioning. In addition, there are significant post-mortem changes, such as retinal detachment, that will confound interpretation of even the best post-mortem images, thus limiting our perspective of the pre-mortem pathology [41]. Additional comparisons are needed from images of comparable conditions from donor eyes and living patients to settle the “fact versus artifact” question.

SDOCT was useful in identifying preretinal, intraretinal and subretinal pathology, as well as imaging individual druse. However, matching SDOCT B-scans to their corresponding histology images was sometimes difficult due to tissue misalignment during sectioning and tissue artifacts. These artifacts included tissue shrinkage and swelling and/or retinal detachment, which made it challenging to align the serial sections into a summed image for localizing very small subretinal pathology such as individual druse. Nevertheless, we found close correlation between SDOCT and histology images.

Summing multiple images decreases the background variance. Collecting multiple images is very time-consuming and limited by the computer memory. For eye 2 and eye 5, the variance decreased as a function of the number of summed images. The relationship reached a plateau at approximately 100 images. With the processing advancement in the handheld commercial system, single images of fixed tissue showed improved definition of layers.

The SDOCT images were used to identify AMD pathology in three of the four AMD patients. The lack of detection in eye 4 may have resulted from inaccurate patient history from the donor family. The SDOCT images from eye 2 showed AMD pathology at the macula, which was validated with histology to be CNV. The SDOCT images from eye 3 showed peripapillary disease, vitreous separation, and a macular cyst, which were also validated with histology. The three “drusen” identified on SDOCT outside the macula, were not detected in the step serial-sections. Thus, the SDOCT reader may have called drusen where none were present, or more likely the less than 200 μm lesion was missed with sectioning. The SDOCT images from eye 7 showed AMD pathology including numerous drusen, in a patient not previously diagnosed with AMD. Despite the confounding choroidal folds, focal domed RPE lesions in areas without choroidal folds appeared on SDOCT images in sites where drusen were detected by light microscopy. Multiple drusen were larger than 125 μm, which is consistent with a level 3 AMD based on AREDS classification [43].

A larger study would be needed to validate using SDOCT imaging for clinical pathology, where accurate diagnosis is critical. Such a study would include histopathology of multiple diseased and control eyes. In this small study, the quality of the SDOCT images allowed for correlation with the histological sections, which is useful for future research. The quality of these images and imaging protocol is not yet optimized to be used in clinical pathology.

SDOCT imaging of postmortem eyecups is a useful, potentially high-throughput, noninvasive, screening method for human donor eyes. SDOCT allows for imaging and

detecting pathology, which can help to confirm clinical diagnosis, to categorize donor eyes by phenotype, and to identify regions of interest for histological sectioning in research. As demonstrated in this small study, the clinical records may be missing or erroneous, which can be misleading for our future research. Thus, there is a critical need for SDOCT as a postmortem efficient and noninvasive screening tool for research in human donor eyes.

Acknowledgments

Authors acknowledge the contributions of Far-shid Guilak for critically reviewing the study proposal; Elizabeth Williams, Ramiro Maldonado, and Katrina Winter for collecting data; Sina Farsiu and Bradley Bower for serving as scientific advisors.

We gratefully acknowledge the financial support of the NIH under grant EB01630 (Brown), 5R21EY017393–02 (McCall, Izatt, Toth), and NEI P30EY005722 in addition to the Macular Vision Research Foundation (Bowes-Rickman), the Ruth and Milton Steinbach Fund (Bowes-Rickman), and the Research to Prevent Blindness William and Mary Greve Special Scholars Award (Bowes-Rickman).

References

1. Puliafito CA, Hee MR, Lin CP, Reichel E, Schuman JS, Duker JS, Izatt JA, Swanson EA, Fujimoto JG. Imaging of macular diseases with optical coherence tomography. Ophthalmology. 1995; 102:217–229. [PubMed: 7862410]
2. Hee MR, Izatt JA, Swanson EA, Huang D, Schuman JS, Lin CP, Puliafito CA, Fujimoto JG. Optical coherence tomography of the human retina. Arch Ophthalmol. 1995; 113:325–332.10.1001/archopht.113.3.325 [PubMed: 7887846]
3. Gloesmann M, Hermann B, Schubert C, Sattmann H, Ahnelt PK, Drexler W. Histologic correlation of pig retina radial stratification with ultrahigh-resolution optical coherence tomography. Invest Ophthalmol Vis Sci. 2003; 44:1696–1703.10.1167/iovs.02–0654 [PubMed: 12657611]
4. Huang D, Swanson EA, Lin CP, Schuman JS, Stinson WG, Chang W, Hee MR, Flotte T, Gregory K, Puliafito CA, Fujimoto JG. Optical coherence tomography. Science. 1991; 254:1178–1182.10.1126/science.1957169 [PubMed: 1957169]
5. Toth CA, Narayan DG, Boppart SA, Hee MR, Fujimoto JG, Birngruber R, Cain CP, DiCarlo CD, Roach WP. A comparison of retinal morphology viewed by optical coherence tomography and by light microscopy. Arch Ophthalmol. 1997; 115:1425–1428.10.1001/archopht.115.11.1425 [PubMed: 9366674]
6. Huang Y, Cideciyan AV, Papastergiou GI, Banin E, Semple-Rowland SL, Milam AH, Jacobson SG. Relation of optical coherence tomography to microanatomy in normal and rd chickens. Invest Ophthalmol Vis Sci. 1998; 39:2405–2416. [PubMed: 9804149]
7. Chauhan DS, Marshall J. The interpretation of optical coherence tomography images of the retina. Invest Ophthalmol Vis Sci. 1999; 40:2332–2342. [PubMed: 10476800]
8. Fukuchi T, Takahashi K, Shou K, Matsumura M. Optical coherence tomography (OCT) findings in normal retina and laser-induced choroidal neovascularization in rats. Graefes Arch Clin Exp Ophthalmol. 2001; 239:41–46.10.1007/s004170000205 [PubMed: 11271460]
9. Furutani Y, Kato A, Yasue H, Alexander LJ, Beattie CW, Hirose S. Evolution of the trappin multigene family in the Suidae. J Biochem. 1998; 124:491–502. [PubMed: 9722657]
10. Li Q, Timmers AM, Hunter K, Gonzalez-Pola C, Lewin AS, Reitze DH, Hauswirth WW. Noninvasive imaging by optical coherence tomography to monitor retinal degeneration in the mouse. Invest Ophthalmol Vis Sci. 2001; 42:2981–2989. [PubMed: 11687546]
11. Horio N, Kachi S, Hori K, Okamoto Y, Yamamoto E, Terasaki H, Miyake Y. Progressive change of optical coherence tomography scans in retinal degeneration slow mice. Arch Ophthalmol. 2001; 119:1329–1332.10.1001/archopht.119.9.1329 [PubMed: 11545639]
12. Ghazi NG, Dibernardo C, Ying HS, Mori K, Gehlbach PL. Optical coherence tomography of enucleated human eye specimens with histological correlation: origin of the outer “red line”. Am J Ophthalmol. 2006; 141:719–726.10.1016/j.ajo.2005.10.019 [PubMed: 16564808]

13. Ghazi NG, Knape RM. Optical coherence tomography of peripheral retinal lesions in enucleated human eye specimens with histologic correlation II. Curr Eye Res. 2006; 31:1047–1049.10.1080/02713680601013033 [PubMed: 17169843]
14. Chen TC, Cense B, Miller JW, Rubin PA, Deschler DG, Gragoudas ES, de Boer JF. Histologic correlation of in vivo optical coherence tomography images of the human retina. Am J Ophthalmol. 2006; 141:1165–1168.10.1016/j.ajo.2006.01.086 [PubMed: 16765704]
15. Ghazi NG, Dibernardo C, Ying H, Mori K, Gehlbach PL. Optical coherence tomography of peripheral retinal lesions in enucleated human eye specimens with histologic correlation. Am J Ophthalmol. 2006; 141:740–742.10.1016/j.ajo.2005.10.058 [PubMed: 16564813]
16. Toth C, Birngruber R, Boppart S, Hee M, Fujimoto J, DiCarlo C, Swanson E, Cain C, Narayan D, Noojin G, Roach W. Argon laser retinal lesions evaluated in vivo by optical coherence tomography. Am J Ophthalmol. 1997; 123:188–198. [PubMed: 9186124]
17. Ruggeri M, Wehbe H, Jiao S, Gregori G, Jockovich ME, Hackam A, Duan Y, Puliafito CA. In vivo three-dimensional high-resolution imaging of rodent retina with spectral-domain optical coherence tomography. Invest Ophthalmol Vis Sci. 2007; 48:1808–1814.10.1167/iovs.06–0815 [PubMed: 17389515]
18. Srinivasan VJ, Ko TH, Wojtkowski M, Carvalho M, Clermont A, Bursell S-E, Song QH, Lem J, Duker JS, Schuman JS, Fujimoto JG. Noninvasive volumetric imaging and morphometry of the rodent retina with high-speed, ultrahigh-resolution optical coherence tomography. Invest Ophthalmol Vis Sci. 2006; 47:5522–5528.10.1167/iovs.06–0195 [PubMed: 17122144]
19. Hausler G, Lindner MW. Coherence radar and spectral radar-new tools for dermatological diagnosis. J Biomed Opt. 1998; 3:21–31.10.1117/1.429899 [PubMed: 23015002]
20. Fercher AF, Hitzenberger CK, Kamp G, El-Zaiat SY. Measurement of intraocular distances by backscattering spectral interferometry. Opt Commun. 1995; 117:43–48.10.1016/0030–4018(95)00119-S
21. Wojtkowski M, Leitgeb R, Kowalczyk A, Bajraszewski T, Fercher AF. In vivo human retinal imaging by fourier domain optical coherence tomography. J Biomed Opt. 2002; 7:457–463.10.1117/1.1482379 [PubMed: 12175297]
22. Chen TC, Cense B, Pierce MC, Nassif N, Park BH, Yun SH, White BR, Bouma BE, Tearney GJ, de Boer JF. Spectral domain optical coherence tomography: ultra-high speed, ultra-high resolution ophthalmic imaging. Arch Ophthalmol. 2005; 123:1715–1720.10.1001/archopht.123.12.1715 [PubMed: 16344444]
23. Stopa M, Bower BA, Davies E, Izatt JA, Toth CA. Correlation of pathologic features in spectral domain oct imaging with conventional retinal studies. Retina. 2008; 28:298–308. [PubMed: 18301035]
24. Mujat M, Chan R, Cense B, Park B, Joo C, Akkin T, Chen T, de Boer J. Retinal nerve fiber layer thickness map determined from optical coherence tomography images. Opt Express. 2005; 13:9480–9491.10.1364/OPEX.13.009480 [PubMed: 19503151]
25. Khanifar AA, Koreishi AF, Izatt JA, Toth CA. Drusen ultrastructure imaging with spectral domain optical coherence tomography in age-related macular degeneration. Ophthalmology. 2008; 115:1883–1890. e1881. [PubMed: 18722666]
26. Banks CN, Hutton WK. Blindness in new south wales an estimate of the prevalence and some of the contributing causes. Aust J Ophthalmol. 1981; 9:285–288.10.1111/j.1442-9071.1981.tb00923.x [PubMed: 7342925]
27. Hyman LG, Lilienfeld AM, Ferris FL, Fine SL. Senile macular degeneration: a case-control study. Am J Epidemiol. 1983; 118:213–227. [PubMed: 6881127]
28. Klein R, Klein BE, Jensen SC, Meuer SM. The five-year incidence and progression of age-related maculopathy: the beaver dam eye study. Ophthalmology. 1997; 104:7–21. [PubMed: 9022098]
29. Klein R, Davis MD, Magli YL, Segal P, Klein BE, Hubbard L. The wisconsin age-related maculopathy grading system. Ophthalmology. 1991; 98:1128–1134. [PubMed: 1843453]
30. Leibowitz HM, Krueger DE, Maunder LR, Milton RC, Kini MM, Kahn HA, Nickerson RJ, Pool J, Colton TL, Ganley JP, Loewenstein JI, Dawber TR. The framingham eye study monograph: an ophthalmological and epidemiological study of cataract, glaucoma, diabetic retinopathy, macular

degeneration, and visual acuity in a general population of 2631 adults, 1973–1975. Surv Ophthalmol. 1980; 24:335–610.10.1016/0039-6257(80) 90015-6 [PubMed: 7444756]

31. National Advisory Eye Council. A National Plan. US Department of Health and Human Services, National Institutes of Health; 1983. Vision Research; p. 12-14.
32. Sommer A, Tielsch JM, Katz J, Quigley HA, Gottsch JD, Javitt JC, Martone JF, Royall RM, Witt KA, Ezrine S. Racial differences in the cause-specific prevalence of blindness in east Baltimore. N Engl J Med. 1991; 325:1412–1417. [PubMed: 1922252]
33. Spraul CW, Grossniklaus HE. Characteristics of drusen and bruch's membrane in postmortem eyes with age-related macular degeneration. Arch Ophthalmol. 1997; 115:267–273.10.1001/archopht. 115.2.267 [PubMed: 9046265]
34. Rudolf M, Clark ME, Chimento MF, Li C-M, Medeiros NE, Curcio CA. Prevalence and morphology of druse types in the macula and periphery of eyes with age-related maculopathy. Invest Ophthalmol Vis Sci. 2008; 49:1200–1209.10.1167/iovs.07-1466 [PubMed: 18326750]
35. Curcio CA, Medeiros NE, Millican CL. The alabama age-related macular degeneration grading system for donor eyes. Invest Ophthalmol Vis Sci. 1998; 39:1085–1096. [PubMed: 9620067]
36. Olsen TW, Feng X. The minnesota grading system of eye bank eyes for age-related macular degeneration. Invest Ophthalmol Vis Sci. 2004; 45:4484–4490.10.1167/iovs.04-0342 [PubMed: 15557458]
37. Scott AW, Farsiu S, Enyedi LB, Wallace DK, Toth CA. Imaging the infant retina with a hand-held spectral-domain optical coherence tomography device. Am J Ophthalmol. 2009; 147(2):364–373. e2. [PubMed: 18848317]
38. Abramoff M, Magelhaes PJ, Ram SJ. Image processing with image. J Biophotonic Int. 2004; 11:36–42.
39. Adler DC, Ko TH, Fujimoto JG. Speckle reduction in optical coherence tomography images by use of a spatially adaptive wavelet filter. Opt Lett. 2004; 29:2878–2880.10.1364/OL.29.002878 [PubMed: 15645810]
40. Jiao S, Knighton R, Huang X, Gregori G, Puliafito C. Simultaneous acquisition of sectional and fundus ophthalmic images with spectral-domain optical coherence tomography. Opt Express. 2005; 13:444.10.1364/OPEX.13.000444 [PubMed: 19488371]
41. Curcio CA. Imaging maculopathy in post-mortem human eyes. Vision Res. 2005; 45:3496–3503.10.1016/j.visres.2005.07.038 [PubMed: 16171840]
42. McCall M, Harkrider CJ, Deramo V, Bailey SF, Winter KP, Rockwell BA, Stolarski DJ, Toth CA. Using optical coherence tomography to elucidate the impact of fixation on retinal laser pathology. Proc SPIE. 2001; 4257:142–148.10.1117/12.434698
43. The age-related eye disease study system for classifying age-related macular degeneration from stereoscopic color fundus photographs: the age-related eye disease study report number 6. Am J Ophthalmol. 132:668–681.10.1016/S0002-9394(01)01218-1 [PubMed: 11704028]

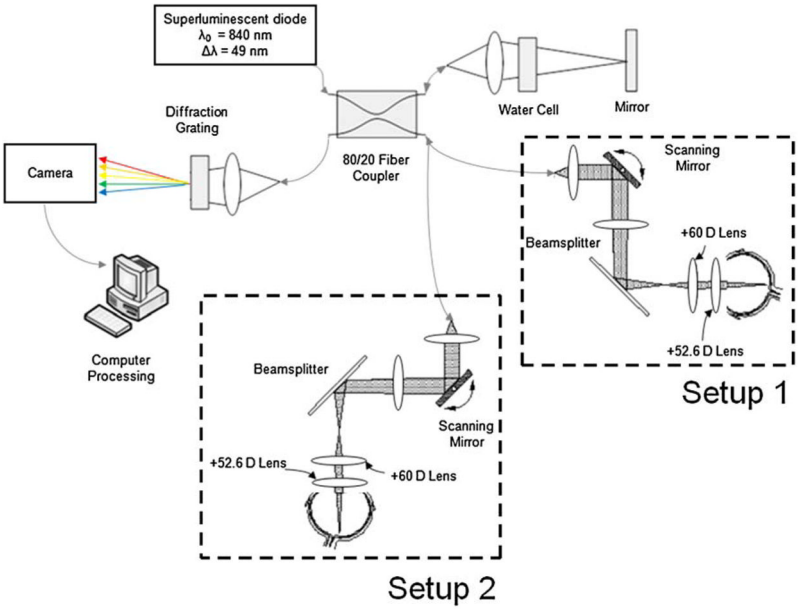

Fig. 1.

The SDOCT system had a superluminescent diode light source, which was split using an 80/20 fiber coupler to the sample arm and the reference arm respectively. In the sample arm, the 52.6 diopter lens was used to focus light onto the eyecup. The reflected light from both arms was diffracted onto a camera and processed. In *Setup 1*, the eyecup is imaged hortzontally. In *Setup 2* the eyecup is imaged from vertically above using the handheld probe

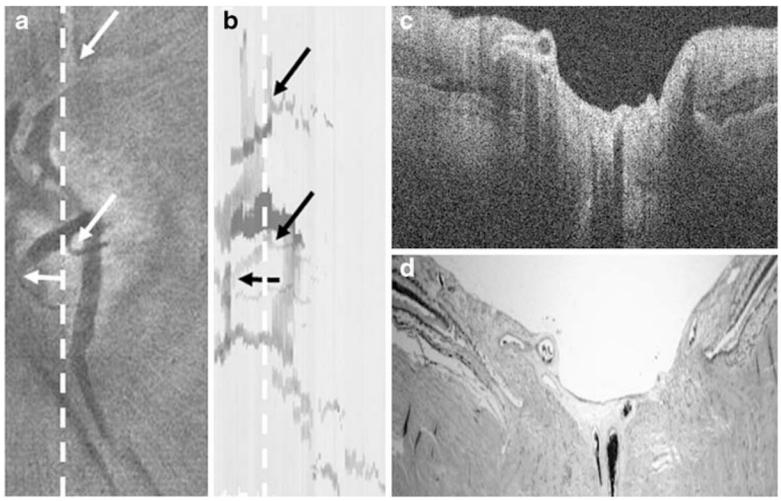

Fig. 2.

SVP with histology images in eye 3. The SDOCT SVP (**a**) and histological summed vessel pattern (**b**) are comparable. The branching of the retinal vessels (*arrows*) are visible in both images. The vessel pattern were marked using Amira. The irregularity of the histological vessel pattern is due to tissue processing and sectioning. Single B-scan (**c**) and light micrograph (**d**) with large arteries in the optic disc corresponding to the *dashed line* in the SVP

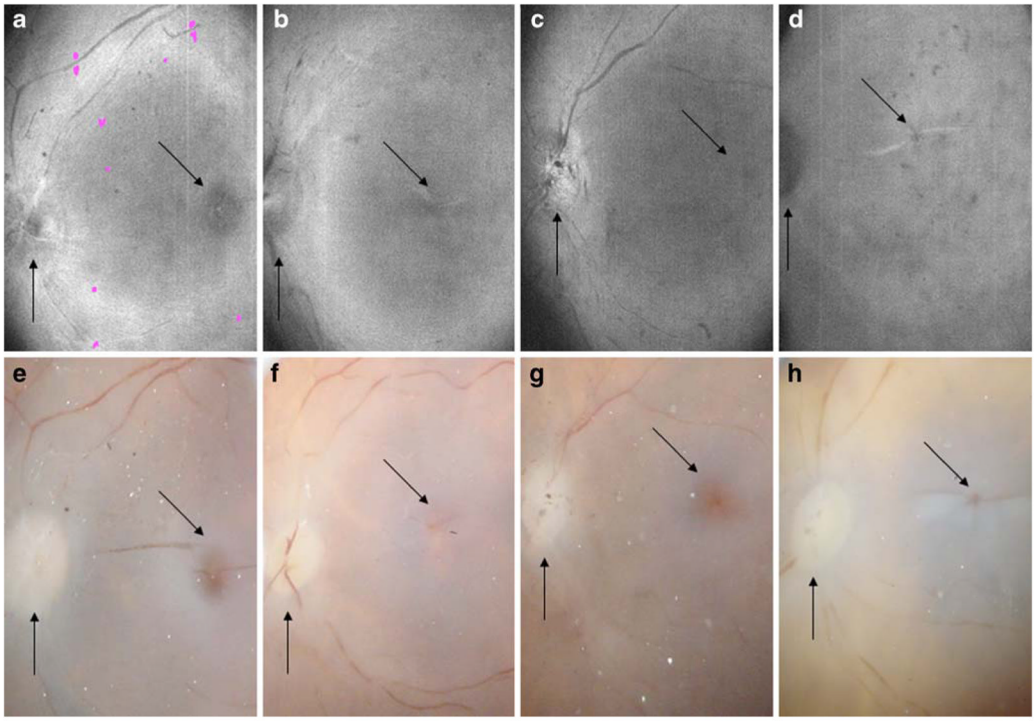

Fig. 3.

SDOCT SVP images (**a–d**) with post-mortem fundus photographs (**e–h**) of eyes 1, 4, 5, and 6. *Vertical arrows* show the optic disc. *Diagonal arrows* show the macula. Vitreous debris casts a shadow resulting in the *grey mottled spots* on the SVP. The drusen are shown in *pink* (**a**)

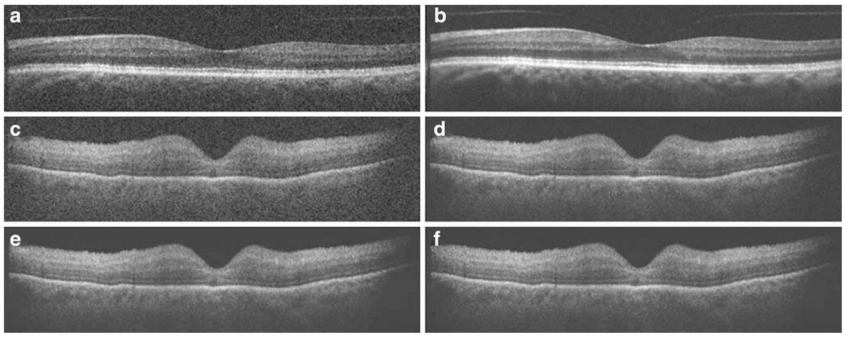

Fig. 4.

Comparison of un-summed (**a,c**) and summed (**b,d,e,f**) SDOCT B-scans. **a,b** B-scans in vivo images of a normal adult eye from (**a**) a single un-summed B-scan and (**b**) 15 summed B-scans. **c–f** B-scans images of a formalin-fixed eye from (**c**) a single un-summed B-scan, (**d**) 15 summed B-scans, (**e**) 100 summed B-scans, and (**f**) 800 summed B-scans. There is little difference in the variance in 100 and 800 summed B-scans. The original 1000×504 pixel images were cropped horitzontally and vertically to 1000×256 respectively

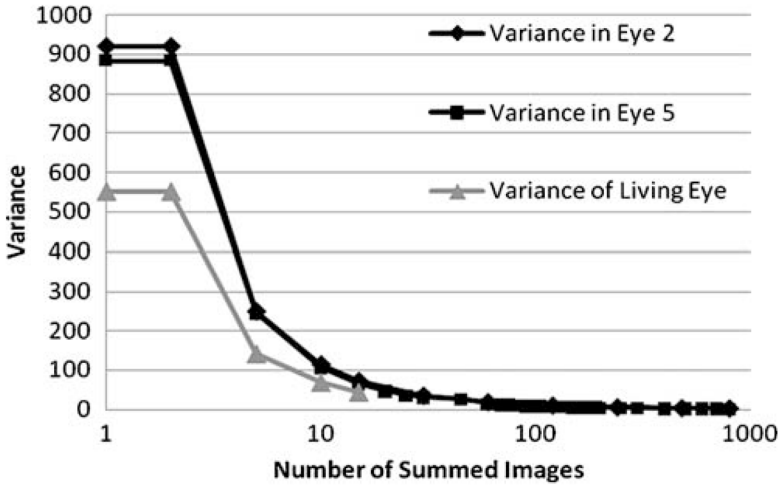

Fig. 5.

Variance in eye 2, eye 5, and living eye. The variance decreases as a function of number of summed images (log scale) to reach a plateau at approximetely 100 summed images. The single image in the living eye has less background variance

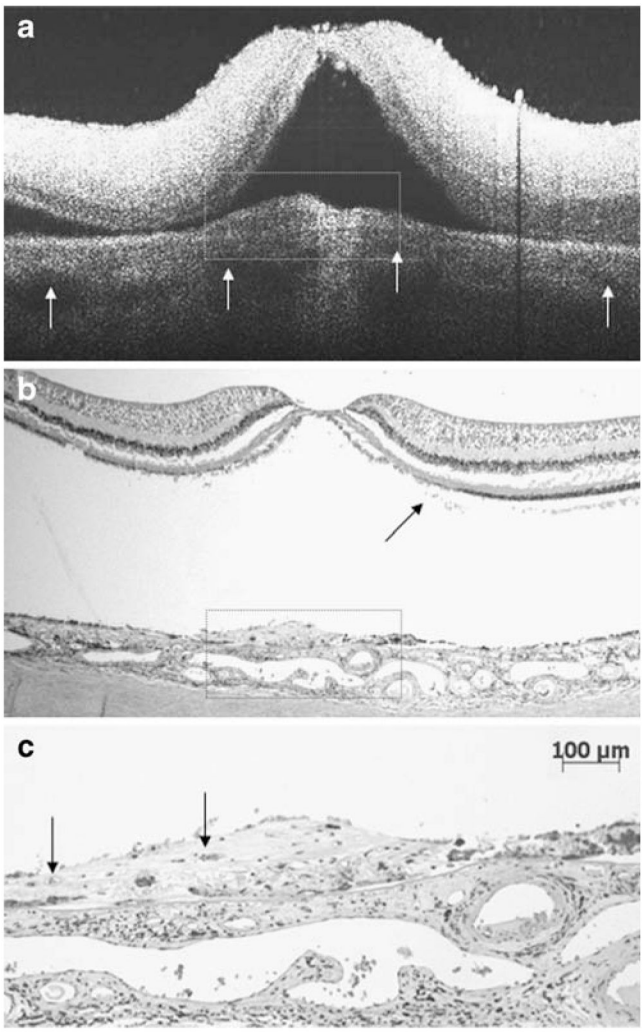

Fig. 6.

SDOCT and histology images from eye 2 with CNV. **a** Summed B-scan showing the CNV under the fovea (*boxed*). The hyporeflective pattern of the large vessels of the choroid can also be visualized (*white arrows*). **b** Light micrograph with CNV under the fovea (2.5×). The retina detached during histological preparation, but the subretinal debris (*arrow*) extending laterally to the site of CNV, suggested previous subretinal fluid. **c** 10× magnification (*boxed* in **b**) with *arrows* showing the blood vessels

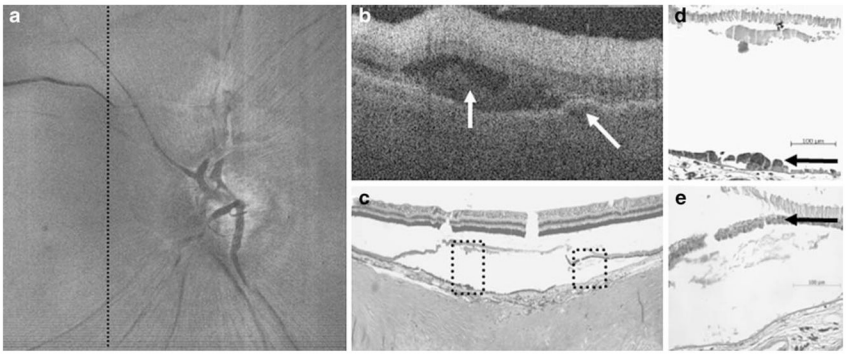

Fig. 7.

SDOCT and histology images from eye 3 with peripapillary disease. **a** 5×5 mm SVP of the nerve. **b** A single unsummed B-scan corresponding to the black dotted line in the SVP shows subretinal "fluid" with mixed hyper- and hyporeflective material above the RPE (*vertical arrow*) and an adjacent apparent RPE detachment (*diagonal arrow*), likely a CNV complex nasal to the nerve. **c** Light micrograph confirmed subretinal (*left box*) and sub-RPE serosanguinous fluid (*right box*). **d** 40× magnification of the left box shows subretinal serosanguinous fluid; **e** 40× magnification of the right box shows sub-RPE fluid (*arrows* mark the RPE)

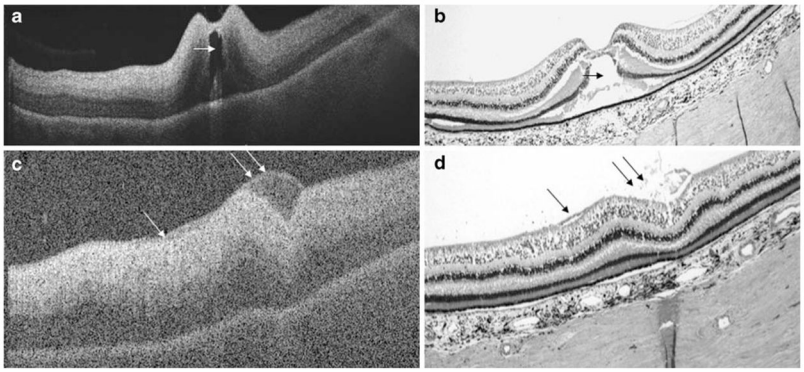

Fig. 8.

SDOCT and histology images from eye 3 with macular cyst and preretinal exudate. **a** 10 mm SDOCT summed image of a macular cyst (*arrow*). **b** Light micrograph of the cyst in the fovea (*arrow*). **c** 5 mm single unsummed SDOCT image of a vitreous separation (*arrows*). **d** Light micrograph of vitreous separation (*arrows*). Preretinal reflective pocket in the SCOCT image (*double arrows*, **c**) corresponded to preretinal cellular exudates (*double arrows*, **d**)

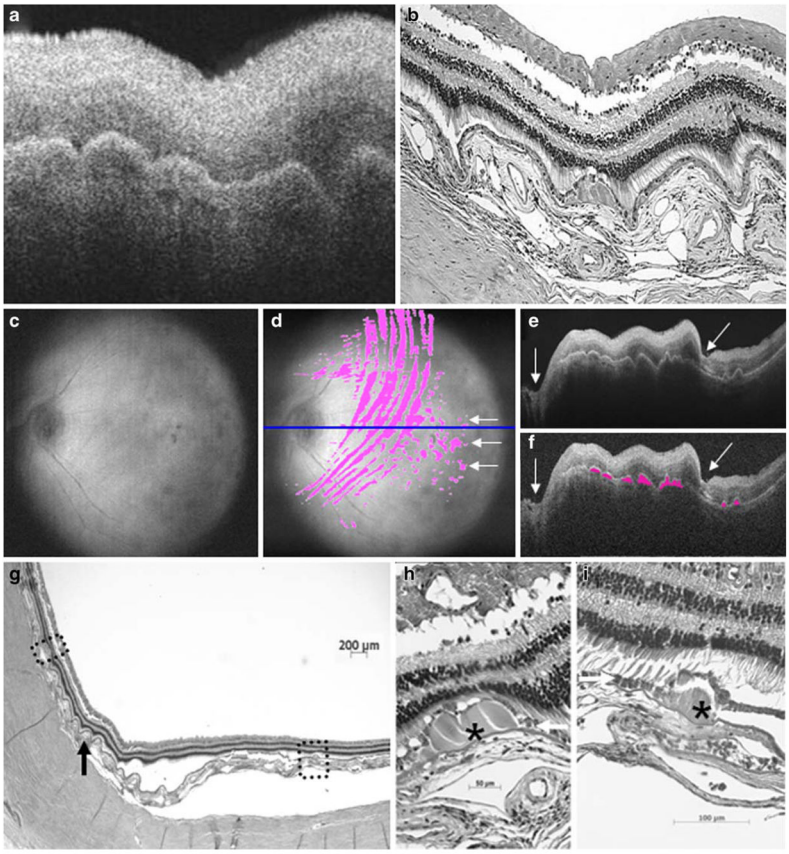

Fig. 9.

SDOCT and histology images of eye 7 with choroidal folds. **a** SDOCT image of domed irregular RPE elevation and hyporeflective choroidal vessels. **b** Light micrograph with corresponding choroidal folds and vessels. **c** Registered 10×10 mm SVP. **d** Marked SVP with the pathology annotated in *pink*. The large arcs of choroidal folds can be distinguished from the drusen (*arrows*). The *blue line* in the marked SVP is the location of the (**e**) summed and (**f**) marked B-scans. Optic nerve (*vertical arrows*) and fovea (*diagonal arrows*) are shown with (**f**) choroidal folds and drusen annotated in *pink*. (**g**) Choroidal folds (*arrow*) and tissue seperation prevented accurate correlation with SDOCT images. (**h**) Large druse (*asterisk*), greater than 125 μm diameter, in the region of choroidal folds and (**i**) smaller druse (*asterisk*) away from the high choroidal folds (*arrows* mark the RPE)

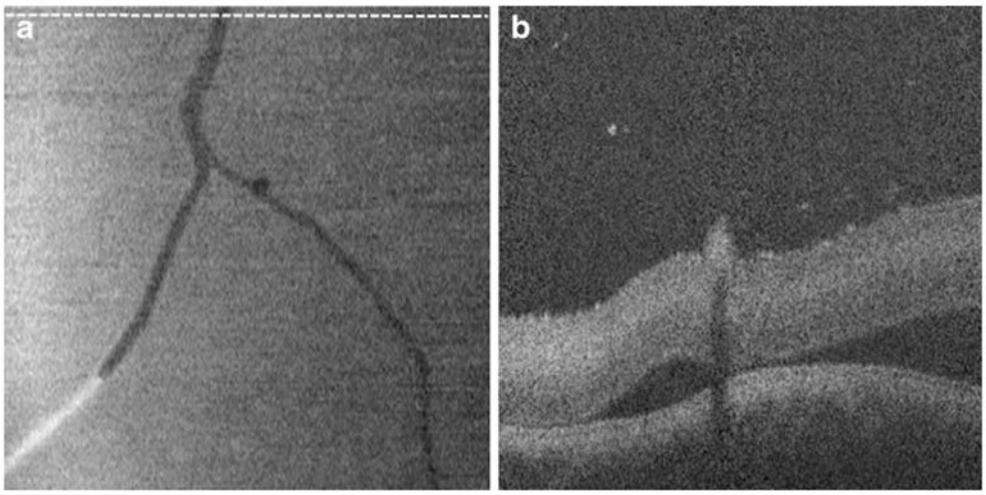

Fig. 10.

SDOCT images of pig eye using handheld probe. **a** 10×10 mm SVP of the posterior eye cup of a pig eye. The *white dotted line* in the marked SVP is the location of the (**b**) unsummed B-scan

Table 1

Human donor eyes for SDOCT study

Eye #	Age (years)	Sex	Death to procurement (hours)	History of AMD	Globe	VA	Clinical history	Clinical history source
1	58	M	9	Y	OS	20/200	Possible early AMD, decrease in VA	E
2	58	M	9	Y	OD	20/200	Possible early AMD, decrease in VA	E
3	69	M	8	Y	OS	Unk	Macular degeneration	F
4	61	M	5	Y	OD	Unk	Macular degeneration	F
5	77	M	3	N	OD	Unk	Cataract	M
6	78	M	3	N	OD	Unk	Hypercholesterolemia	M
7	67	M	3	N	OD	Unk	Scleral buckle, retinal detachment	M

VA = visual acuity, *Unk* = unknown, *E* = eye exam, *F* = family report, *M* = medical record

Table 2

SDOCT morphology and comparison to histopathology findings

Eye #	SDOCT findings	Histopathology findings	Figure #
1	Multiple collections of drusen	ND	3
2	a) Three collections of drusen	a) Not detected	
	b) Subfoveal lesion	b) Choroidal neovascularization	6
	c) Subretinal fluid	c) Retinal separation at fovea with processing artifact	6
3	a) Single collection of drusen	a) Not detected	
	b) RPE elevation	b) Sub-RPE exudates	7
	c) Subretinal fluid and reflectivity	c) Subretinal serosanguinous exudates	7
	d) Epiretinal membrane with macular pucker with reflective preretinal material	d) Epiretinal membrane with preretinal exudates containing cellular debris	8
	e) Macular cyst with retinal thickening	e) Macular cyst with retinal thickening	8
4	Wrinkle in RPE	ND	3
5	Normal fixed tissue	ND	3
6	Wrinkle in RPE	ND	3
7	a) Choroidal folds with apparent postmortem artifact from compression of globe prior to fixation	a) Choroidal folds consistent with SDOCT	10, 11
	b) Multiple collections of drusen	b) Multiple collections of drusen	11, 12

ND = not done, *RPE* = retinal pigment epithelium